PAPER

Synergistic melamine intercalation and Zn(NO₃)₂ activation of N-doped porous carbon supported Fe/Fe₃O₄ for efficient electrocatalytic oxygen reduction†

Yaoyao Ni,[a] Tingjuan Wang,[a] Yan Zhou,[a] Chao Wang,[a] Yingwen Tang,[b] Tao Li[c] and Baoyou Geng [ID] *[ad]

Developing inexpensive, efficient and good stability transition metal-based oxygen reduction reaction (ORR) electrocatalysts is a research topic of great concern in the commercial application of fuel cells. Herein, with zinc nitrate as activator, iron nitrate as active component and melamine as intercalating agent and nitrogen source, an N-doped porous carbon supported Fe/Fe₃O₄ (Fe/Fe₃O₄@NC) catalyst is successfully synthesized by an impregnation–calcination method combined with freeze-drying technique. The positive onset potential (E_{onset}), half-wave potential ($E_{1/2}$) and limiting current density (J_L) of the optimal Fe/Fe₃O₄@NC catalyst are 1.012, 0.90 V $vs.$ RHE and 5.87 mA cm^{-2}, respectively. Furthermore, Fe/Fe₃O₄@NC catalyzes ORR mainly through a 4e$^-$ pathway, and the yield of H₂O₂ is less than 5%. It also manifests a robust stability after 5000 CV cycles of ADT testing, and the half-wave potential is only negatively shifted 17 mV. The structural characterization and experimental results further suggest that the outstanding ORR electrocatalytic performance of the Fe/Fe₃O₄@NC catalyst benefits from the synergetic effect of zinc nitrate activation and nitrogen doping, which can greatly improve the specific surface area, thus better dispersing more metal active sites. This work puts forward a simple and practicable way for preparing high-performance non-noble metal-based biomass ORR electrocatalysts.

1. Introduction

Extensive use of fossil fuels has caused severe energy and environmental problems, thus the exploration of alternative renewable energy or energy conversion and storage technology has aroused widespread concern.[1–3] Among them, fuel cells have attracted great research interest due to their high energy density and green economy. Nevertheless, as the cathode reaction of fuel cells and metal–air batteries, the oxygen reduction reaction (ORR) also displays some problems, such as inherent sluggish kinetics and high overpotential, which greatly reduces its working efficiency.[4,5] Up to now, Pt-based catalysts have been recognized as the best ORR electrocatalysts, whereas the large-

scale application in fuel cells is still limited by the scarce resources, high cost and poor stability, *etc.*[6,7] To overcome these issues, great efforts have been made to explore the non-noble metal catalysts with inexpensive, earth-abundant and good electrochemical activity. In recent years, researchers have turned their research direction to the transition metals (such as Fe, Co, Ni, Mn, *etc.*)-based ORR electrocatalysts. Meanwhile, they found that heteroatoms (such as N, B, P, S, *etc.*)-doping into carbon materials can significantly change the carbon composition and electron distribution due to the different electronegativity of heteroatoms.[8–12] The rational design of heteroatom-doped carbon can effectively improve O₂ adsorption, weaken O–O bond and greatly enhance the electrocatalytic performance of ORR, which has gradually become an attractive topic in fuel cell research.[13] In particular, recently reported iron and nitrogen doped carbon (Fe/N/C) and N-doped carbon supported transition metal oxides have been universally used in high-performance ORR catalysts.[14,15]

Among various carbon-based materials, it is crucial to choose suitable conductive carbon materials (such as graphene, CNTs and MOFs) as supports to improve ORR activity. Nevertheless, their large-scale commercial application is hindered by the high price and complicated processes.[16–18] Recently, biomass materials have emerged as a rising alternative carbon

[a]College of Chemistry and Materials Science, The Key Laboratory of Electrochemical Clean Energy of Anhui Higher Education Institutes, Anhui Provincial Engineering Laboratory for New-Energy Vehicle Battery Energy-Storage Materials, Anhui Normal University, No. 189 Jiuhua South Road, Wuhu, 241002, China. E-mail: bygeng@mail.ahnu.edu.cn

[b]College of Physics and Information Engineering, Minnan Normal University, China

[c]Shanghai Institute of Technical Physics, Chinese Academy of Sciences, China

[d]Institute of Energy, Hefei Comprehensive National Science Center, Anhui, Hefei, China

† Electronic supplementary information (ESI) available. See https://doi.org/10.1039/d2ra02170f

material due to its advantages of low cost, sustainability and structural diversity.[19–22] Accordingly, in order to obtain the equal or superior electrocatalytic ORR performance to commercial Pt/C catalyst, it is feasible to introduce transition metals (such as Fe) into the N-doped biomass materials to form more active sites by modifying the electronic structures of carbon matrix. Zhang and co-workers prepared Fe, N co-doped graphite carbon high-efficiency ORR electrocatalyst with carbon nanodots derived from shrimp shells as precursors, which shows better ORR performance than Pt/C.[23] Due to the dense and thick carbon matrix in some biomass carbon materials, metal nanoparticles tend to agglomerate during high-temperature pyrolysis, so the preparation of carbon materials with high specific surface area and proper pore structure is vitally important for the effective anchoring and dispersion of active components on Fe/N/C catalysts. Activation method is one of the universal methods to synthesize porous carbon materials. KOH, $ZnCl_2$ and H_3PO_4 are considered as universal chemical activators at present.[24–26] Generally, the evaporation of Zn at high temperature promotes the carbonization of carbon materials and increases the degree of defects, which will expand the specific surface area and promote the mass transfer on the electrode/electrolyte interfaces.[27,28] As a typical example, Li *et al.* prepared $ZnCl_2$–Fe/C/N@bio-C and $Zn(NO_3)_2$–Fe/C/N@bio-C electrocatalysts, in which $ZnCl_2$ and $Zn(NO_3)_2$ are used as activating agents to make the Fe-based active species disperse well onto the biomass template.[29] The results reveal that both zinc salts is significant for the formation of special pore structure and carbon defects, but $Zn(NO_3)_2$ has a better advantage in improving the activity toward ORR. The excellent ORR performance of these N-doped iron species biomass composite materials not only benefits from their special structural characteristics, but also the exposure of catalytic active sites and the improvement of mass transfer efficiency.

Additionally, melamine is currently taken as a nitrogen source for preparing N-doped carbon materials because of its high nitrogen content and easy availability.[30] It is found that the graphitization degree, porosity and conductivity of Fe/N/C catalysts are effectively improved by introducing melamine in the preparation process.[31–33] Besides, it can be seen that using melamine as ligand to prepare catalysts can significantly enhance the ORR catalytic performance.[34] Most of these catalysts pyrolyze at high temperature, various active substances are produced besides the Fe–N_x coordination active site, such as metallic Fe/Fe_3C nanoparticles, Fe_xO_y or FeN_x nanoparticles and so on.[35,36] The incorporation of melamine into carbon carriers possesses a unique potential in regulating the active sites of ORR electrocatalyst. The prepared porous carbon support can not only better disperse the metal active sites, but also averts the aggregation of nanoparticles during pyrolysis. It is believed that the synergistic effect of N-doped carbon and iron species active sites is helpful to optimize the ORR performance.[37,38] Therefore, the transition metal based nanoparticles supported by carbon materials are more maneuverable in both the preparation process and the composition and structure regulation.

Herein, we design and develop a facile preparation of N-doped porous carbon supported Fe/Fe_3O_4 composites (Fe/Fe_3O_4@NC) by melamine intercalation with zinc nitrate as activator. The impregnation–calcination method combined with freeze-drying technique can effectively fix active substances and reasonably introduce nitrogen into carbon materials. As electrochemical tests demonstrated, Fe/Fe_3O_4@NC electrocatalyst exhibits high activity toward ORR with positive onset potential, half-wave potential and limiting current density of 1.012, 0.90 V *vs.* RHE and 5.87 mA cm^{-2}, respectively. Moreover, Fe/Fe_3O_4@NC has only a slight negative shift by 17 mV after 5000 CV cycles in the half-wave potential. It shows that the synergistic effect of zinc nitrate activator, Fe/Fe_3O_4 nanoparticles and nitrogen doping is considered as the main factor to promote the electrocatalytic activity, thus showing superior ORR activity and good durability compared with Pt/C. The general strategy is more flexible and scalable for the preparation of other transition metal-based biomass materials because of its low manufacturing cost and easy to operate, which could be suitable for the further large-scale production.

2. Experimental section

2.1. Chemicals and materials

α-Cellulose powder (25 μm, Maklin), $Fe(NO_3)_3 \cdot 9H_2O$ (AR, Sinopharm Chemical Reagent Co), $Zn(NO_3)_2 \cdot 6H_2O$ (AR, Sinopharm Chemical Reagent Co), Melamine (99%, Aladdin), Pt/C (20 wt%, Shanghai Chuxi industrial Co), Al_2O_3 (Gaoss Union), *N,N*-dimethylformamide (DMF) (99.5%, Aladdin), KOH (99.99%, Aladdin), H_2SO_4 (SCR, 95–98%). All reagents were used without any purification.

2.2. Synthesis of catalysts

2.2.1. Fe/Fe_3O_4@NC. 0.2 g α-Cellulose powder was placed in 25 mL DI water, sonicated for 30 min. Subsequently, 0.225 mol $Fe(NO_3)_3 \cdot 9H_2O$ and 1.125 mol $Zn(NO_3)_2 \cdot 6H_2O$ were successively added, stirred for 1 h to obtain uniformly mixed precursor solution. Standing still a whole night at normal atmospheric temperature (between 15 and 25 °C), then freeze-drying at −70 °C for 12 h to remove internal moisture. The precursor powder and melamine in a mass ratio of 1 : 10 were mixed fully and evenly ground in mortar. Then product was annealed at 550 °C for 1 h, 1000 °C for 1 h with a heating rate of 5 °C min^{-1} in argon atmosphere at 80 Sccm. The as-prepared black powder was named Fe/Fe_3O_4@NC.

In addition, other factors such as the amount of metal, pyrolysis temperature and the amount of nitrogen doping will affect the ORR performance. Thus, the performances of ORR were optimized with different metal iron contents with the contents of 0.15, 0.20, 0.225, 0.25 and 0.30 mmol, respectively. As shown in Fig. S6a,† linear sweep voltammetry (LSV) measurements showed that the optimal iron content was 0.225 mmol. The pyrolysis temperature in Ar atmosphere was from 850, 900, 950 to 1000 °C. As shown in Fig. S6b,† LSV measurements showed that the best pyrolysis temperature was 1000 °C. The performances of ORR were further optimized

when the mass ratio of the precursor powder to melamine was 1 : 1, 1 : 5, 1 : 10, 1 : 15 and 1 : 20, respectively. As shown in Fig. S6c,† LSV measurements showed that the best mass ratio was 1 : 10.

2.2.2. Fe/Fe₃O₄@NC (Zn-free). For control experiments, other samples were synthesized by the same steps. The sample synthesized without the addition of the zinc nitrate in the precursor solution was named Fe/Fe₃O₄@NC (Zn-free).

2.2.3. NC (Fe-free). The sample synthesized without the addition of the iron nitrate in the precursor solution was named NC (Fe-free).

2.2.4. Fe/Fe₃O₄@C (N-free). The sample synthesized without melamine during pyrolysis process was named Fe/Fe₃O₄@C (N-free).

2.2.5. Fe₃O₄@NC. The Fe/Fe₃O₄@NC catalyst was refluxed in 2 mol L⁻¹ H₂SO₄ solution at 80 °C for one day, washed to neutrality with DI water, the dried sample named Fe₃O₄@NC.

2.3. Physical characterization

The microstructures, morphology and element composition of the samples were characterized by the scanning electron microscope (SEM, Hitachi, S-8100), transmission electron microscopy (TEM, Hitachi, HT-7700) and high resolution transmission electron microscopy (HRTEM, FEI, Tecnai G220). The selected area electron diffraction (SAED) pattern was acquired on JEM-2010 TEM at 200 kV. X-ray powder diffraction (XRD, Bruker AXS, D8 Advance, Cu Kα). N₂ adsorption–desorption isotherm was measured on Micromeritics ASAP 2020 analyzer at 77 K, in which the Brunauer–Emmett–Teller (BET) and Barrett–Joyner–Halenda (BJH) calculated the specific surface area and pore size distributions of the catalysts. X-ray photoelectron spectroscopy (XPS) was analyzed on Thermo Fiaher Scientific K-Alpha. Raman spectroscopy (RM-inVia) was tested the defects and graphitization degree of the carbon materials with laser excitation wavelength of 532 nm.

2.4. Electrochemical measurements

The electrochemical performance was measured on CHI760E with a three-electrode system. The glassy carbon (GC) disk electrode ($d = 5$ mm), Ag/AgCl (saturated KCl solution) and graphite rod were served as working, reference and counter electrode, respectively. 0.1 M KOH solution is the electrolyte solution. Besides, GC electrode was polished by Al₂O₃. For the convenience of comparison with other literature results, all potentials were diverted to reversible hydrogen electrode (RHE) formula: E (vs. RHE) = E (vs. Ag/AgCl) + 0.059 × pH + 0.197 (0.1 M KOH, pH ≈ 14). The catalyst ink was prepared as follows: 2 mg catalyst or Pt/C and 1 mg carbon (Vulcan XC-72) were ultrasonically dispersed in DI water (660 μL), DMF (330 μL) and 5% Nafion (10 μL) for 30 minutes, 20 μL ink was dropped onto the GC electrode. The cyclic voltammetry (CV) curves were obtained with a scan rate of 20 mV s⁻¹ in Ar- or O₂-saturated electrolyte solution, while the Liner sweep voltammetry (LSV) was tested with 1600 rpm at 10 mV s⁻¹. The LSV background current value under Ar saturation condition was deducted. Accelerated durability test (ADT) for stability was performed by

5000 CV cycles from 0.4 to 1.1 V vs. RHE. When rotating ring disk electrode (RRDE) was regard as working electrode, the number of electrons transfer (n) and hydrogen peroxide yield (H₂O₂%) of the catalysts were based on the equation:

$$n = 4 \times \frac{I_d}{\frac{I_r}{N} + I_d}$$

$$H_2O_2(\%) = 200 \times \frac{\frac{I_r}{N}}{\frac{I_r}{N} + I_d}$$

where, I_r and I_d are the ring current and disk current, respectively. n is the electron transfer number. N is the collection efficiency ($N = 0.37$).

Koutecky–Levich (K–L) equation was used to calculate the kinetic current of ORR:

$$\frac{1}{J} = \frac{1}{J_L} + \frac{1}{J_K} = \frac{1}{B\omega^{\frac{1}{2}}} + \frac{1}{J_K}$$

where, J, J_K and J_L are the measured current, kinetic current and diffusion limiting current densities.

3. Results and discussion

3.1. Physicochemical analysis

The preparation process of Fe/Fe₃O₄@NC electrocatalyst was depicted in Scheme 1. Firstly, in order to better adsorb the mental Fe³⁺ ions, α-cellulose powder was selected as carbon source and ultrasonically dispersed in DI water, then zinc nitrate was added as activator, and homogeneous solution was obtained by impregnation method. Afterward, the precursor powder was obtained by freeze-drying technique. Grinding the precursor powder and melamine in mortar at a certain mass ratio to obtain the uniform mixture. Finally, the powder was pyrolyzed in Ar atmosphere according to the following two-stage heating program: (1) at 550 °C for 1 h to dehydrate and carbonize the material; (2) at 1000 °C for 1 h to further activate and graphitize the material, which is due to the evaporation of zinc at high temperature (>800 °C).[39] The final product of N-doped multilayer two-dimensional porous carbon supported
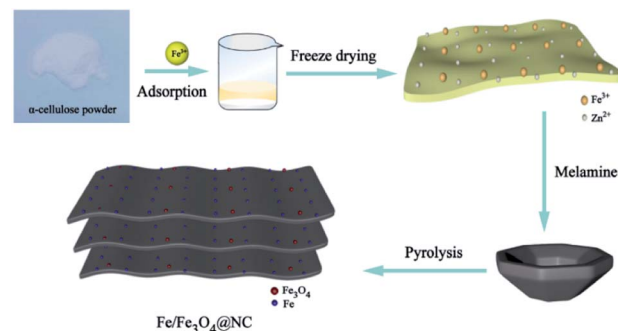
Scheme 1 Schematic diagram of Fe/Fe₃O₄@NC preparation process.

Fe/Fe$_3$O$_4$ composites was successfully prepared, named Fe/Fe$_3$O$_4$@NC.

In addition, the synthesis conditions of different Fe content, pyrolysis temperature and mass ratio of the precursor powder to melamine further optimized the ORR activity. The Liner sweep voltammetry (LSV) measurement and corresponding bar graph was shown in Fig. S7.† For comparison, the samples of Fe/Fe$_3$O$_4$@NC (Zn-free), NC (Fe-free), Fe/Fe$_3$O$_4$@C (N-free) and Fe$_3$O$_4$@NC (acid etching) were prepared as details in ESI† of Experimental Section.

The morphology and structure of the samples were analyzed by SEM and TEM. Fig. S1† shows that the unactivated α-cellulose power presents the smooth blocky carbon matrix with almost no pore structure, the thick carbon structure is not conducive to the good dispersion of metal particles to some extent.[40] The precursor that has not been pyrolyzed did not show obvious wrinkles and is prone to internal particle aggregation (in Fig. S2†). As shown in Fig. 1a, the Fe/Fe$_3$O$_4$@NC catalyst possesses the typical graphitization structure with multilayer two-dimensional layered nanosheets melamine as a nitrogen source could be resolved into NH$_3$ gas during the pyrolysis process, which is due to the decomposition of melamine as intercalating agent into NH$_3$ gas during pyrolysis.[41,42] Fig. 1b shows some large particles (d = 100–200 nm) and small particles (d = 10–20 nm) with good dispersion are uniformly embedded in the carbon matrix, while the small particles can be ascribed to the confinement of graphene layers to inhibit the agglomeration of nanoparticles. However, the controllable morphology and structure of sample pyrolyzed by urea instead of melamine is greatly affected without multilayer nano-flake structure, and the metals tend to aggregate into large particles (Fig. S3†). Additionally, the SAED pattern appears distinct diffraction rings, which indicates that Fe/Fe$_3$O$_4$@NC is polycrystalline nature (inset of Fig. 1b). The other four comparative samples such as Fe/Fe$_3$O$_4$@NC (Zn-free), NC (Fe-free), Fe/Fe$_3$O$_4$@C (N-free) and Fe$_3$O$_4$@NC are shown in Fig. S4.† From these images, it can be observed that the interior of the carbon matrix is relatively thick, thus the metal nanoparticles cannot be well dispersed and easy to agglomerate. In view of the fact that zinc nitrate as activator, Zn atoms volatilize completely at high temperature, leaving a large number of pores and activating the carbon substrate, thus resulting in more micropores and defects and the Fe species particles could be better dispersed in the carbon matrix. Meanwhile, iron nitrate possessed a certain etching effect on carbon materials, which promotes the graphitization degree to a certain extent.[43,44] Clearly, Fe$_3$O$_4$@NC catalyst shows a rough porous structure by acid etching, the particles size becomes smaller and well distributed in the porous carbon substrate. The HRTEM image of Fe/Fe$_3$O$_4$@NC reveals that the lattice fringes of 0.25 nm are clearly visible, which is ascribed to the (311) crystal plane of Fe$_3$O$_4$, as shown in Fig. 1c. Moreover, the d-spacing of 0.34 nm around the Fe$_3$O$_4$ nanoparticles, corresponding to the (002) facet of graphitic carbon, the structure of metal nanoparticles coated with graphite carbon can prevent corrosion and aggregation during electrocatalysis.[45] The lattice stripes of the smaller nanoparticles are not obvious, then the d-spacing cannot be clearly calculated, so it is impossible to determine whether they are metallic Fe or not. According to Fig. 1d and e, the STEM and corresponding element mapping images can be observed that Fe, O, N and C elements are homogeneously dispersed in the hybrid material, which illustrates that nitrogen and iron atoms are successfully introduced into the porous carbon materials. In addition, it seems that Fe and O mainly exist in the large particles, while the small particles only contain Fe, it is speculated that these carbon-coated metallic iron species might be elemental iron or iron oxides.[46]
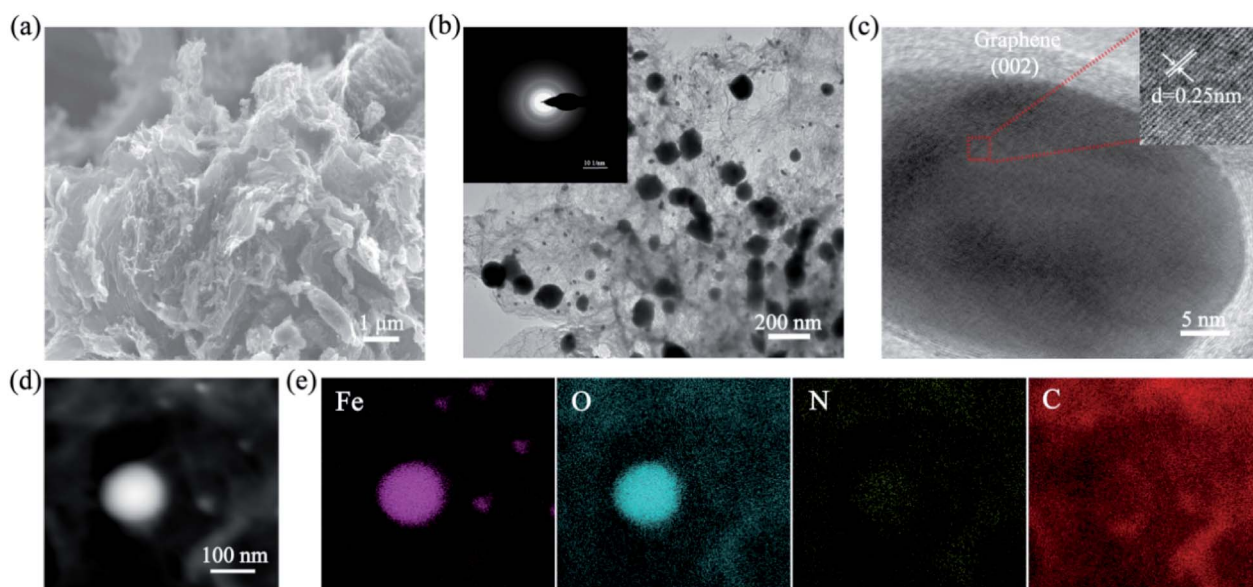

Fig. 1 (a) SEM image of Fe/Fe$_3$O$_4$@NC, (b) TEM image and SAED pattern of Fe/Fe$_3$O$_4$@NC, (c) HRTEM image of Fe/Fe$_3$O$_4$@NC, (d) STEM image of Fe/Fe$_3$O$_4$@NC, (e) corresponding element mapping images of Fe, O, N and C atoms of Fe/Fe$_3$O$_4$@NC.

XRD characterization was applied to analyse the chemical composition and crystal structure of the samples. Fig. 2a shows that the peak of 2θ at 26° is attributed to the graphite carbon (002) phase. The diffraction peak located at 32.1° is attributed to the (311) phase of Fe_3O_4 (JCPD No. 996-0073), and also appears in the other four samples, while the diffraction peak of the detected Fe phase (JCPD No. 996-0064) is weak possibly because of the relatively low loading of Fe or the low content of reduced iron, which is in agreement with the results of HRTEM. It also demonstrates that Fe_3O_4 still exists despite acid leaching, which may be because some Fe_3O_4 nanoparticles are wrapped by the graphitized carbon and cannot be completely removed. The defect structure and graphitization degree of the samples were evaluated by Raman spectroscopy. According to Fig. 2b, there are two characteristic peaks approximately at 1350 and 1590 cm^{-1}, defined as the D band and G band, which represent the structural defects of sp^3 hybridization and the graphitized carbon of sp^2 hybridization, respectively. Moreover, the intensity ratio of D and G band (I_D/I_G) is a vital index to evaluate defect and graphitization degree of the carbon materials.[47] It can be calculated that the value of I_D/I_G of Fe/Fe$_3$O$_4$@NC, Fe/Fe$_3$O$_4$@NC (Zn-free), NC (Fe-free), Fe/Fe$_3$O$_4$@C (N-free) and Fe$_3$O$_4$@NC are 0.98, 1.05, 0.96, 1.11 and 1.01, respectively. As a consequence, the graphitization degree of Fe/Fe$_3$O$_4$@NC is the highest compared with other iron-containing materials, indicating that the addition of zinc nitrate and melamine obviously promotes the formation of graphitization and defect structures of carbon materials, thus endowing these catalysts with good conductivity and stability, which is conducive to improve the electron transfer efficiency in the electrocatalytic ORR process.

The specific surface area and pore size distribution of the samples were analysed by Brunauer–Emmett–Teller (BET) and Barrett–Joyner–Halenda (BJH) methods through the nitrogen adsorption–desorption isotherm at 77 K. As shown in Fig. 3 and S5,† all catalysts show type IV isotherms with H3 hysteresis loop, indicating the appearance of mesoporous structure. Furthermore, the pore structure properties from BET analysis are illustrated in Table S1.†

The specific surface area of Fe/Fe$_3$O$_4$@NC, Fe/Fe$_3$O$_4$@NC (Zn-free), NC (Fe-free), Fe/Fe$_3$O$_4$@C (N-free) and Fe$_3$O$_4$@NC are 546.70, 449.87, 357.91, 302.69 and 242.70 $m^2\ g^{-1}$, respectively. Moreover, the corresponding mesoporous volume ratios are
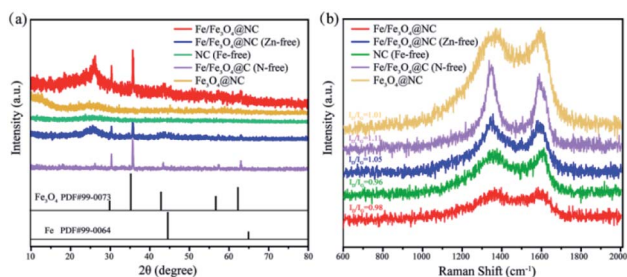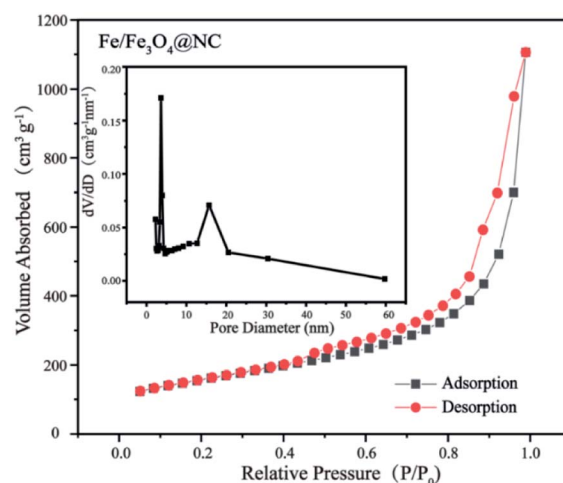

Fig. 3 Nitrogen adsorption–desorption isotherm and pore size distribution of Fe/Fe$_3$O$_4$@NC catalyst.

97.46, 96.86, 93.75, 81.95 and 97.99%, respectively. Notably, the Fe$_3$O$_4$@NC catalyst displays the lowest specific surface area and the highest mesoporous volume ratio, which is attributed to the acid etching. These results indicate that the Fe/Fe$_3$O$_4$@NC catalyst possesses the largest specific surface area and higher mesoporous volume ratio are benefited from the synergistic effect of the activation of zinc nitrate, the etching of carbon materials by iron nitrate and NH_3 generated by the addition of melamine during pyrolysis, which is conducive to expose more active sites and facilitate the rapid mass transfer and electron transfer in ORR electrocatalytic process.

XPS measurements were investigated to further analyse the valence states and chemical composition of the materials. Firstly, the XPS survey spectrum displays that C, N, O and Fe elements exist in Fe/Fe$_3$O$_4$@NC catalyst (Fig. 4a), which is consistent with the results of corresponding element mapping. It is noticed that the relative content of Fe, O and C elements in Fe/Fe$_3$O$_4$@NC (Fe = 24.54%, O = 29.81% and C = 45.65%) and Fe/Fe$_3$O$_4$@C (N-free) (Fe = 24.20%, O = 29.81% and C = 45.99%) catalysts are comparatively close, the difference in composition lies in whether nitrogen is doped or not. According to Fig. 4b, the high resolution Fe 2p XPS spectrum of Fe/Fe$_3$O$_4$@NC catalyst corresponds to Fe^0 at 708.2 and 720.3 eV, Fe^{2+} at 710.9 and 724.0 eV, and Fe^{3+} at 714.1 and 726.4 eV in Fe $2p_{3/2}$ and Fe $2p_{1/2}$, respectively. Besides, there peak is a satellite peak at 718.3 eV, which implies that Fe(II) and Fe(III) ions coexist in those electrocatalysts and proves the existence of Fe_3O_4. The formation of polyvalent iron is mainly due to the sensitivity of metallic iron to air oxidation.[48] In contrast, Fe/Fe$_3$O$_4$@C (N-free) can be classified as Fe^0 at 710.4 and 720.0 eV, Fe^{2+} at 711.3 and 724.5 eV, and Fe^{3+} at 713.2 and 726.3 eV in Fe $2p_{3/2}$ and Fe $2p_{1/2}$, respectively (shown in Fig. 4c). It should be pointed out that the addition of melamine makes the binding energy shift obviously. The relative sensitivity factor method is used to calculate the ratio of Fe/Fe$_3$O$_4$ by the area of the element spectrum peak.[49] Combined with Fig. S6c,† the Fe/Fe$_3$O$_4$ ratios of Fe/Fe$_3$O$_4$@NC, Fe/Fe$_3$O$_4$@NC (Zn-free) and Fe/Fe$_3$O$_4$@C (N-free) catalysts are

Fig. 2 (a) XRD patterns, and (b) Raman spectra of Fe/Fe$_3$O$_4$@NC, Fe/Fe$_3$O$_4$@NC (Zn-free), NC (Fe-free), Fe/Fe$_3$O$_4$@C (N-free) and Fe$_3$O$_4$@NC catalysts.
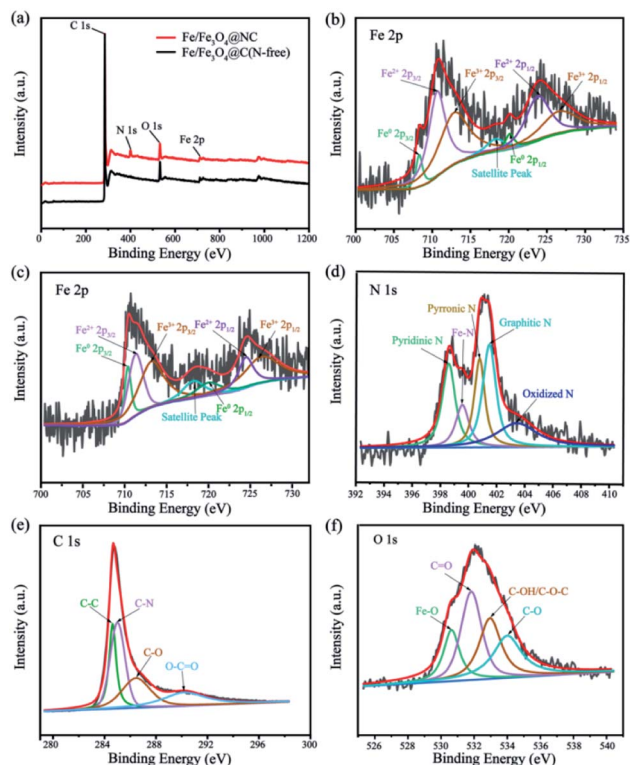
Fig. 4 (a) XPS survey spectra of Fe/Fe$_3$O$_4$@NC and Fe/Fe$_3$O$_4$@C (N-free), (b) high-resolution XPS spectrum of Fe 2p for Fe/Fe$_3$O$_4$@NC and (c) Fe/Fe$_3$O$_4$@C (N-free), (d) N 1s, (e) C 1s, (f) O 1s for Fe/Fe$_3$O$_4$@NC.

close to 1 : 5, elucidating that the products are controllable to some extent. Fig. 4d shows that the Fe/Fe$_3$O$_4$@NC catalyst can be assigned to pyridinic N (398.6 eV), Fe–N$_x$ (399.6 eV), pyrrole N (400.8 eV), graphitic N (401.5 eV) along with oxidized N (403.4 eV). As proved by previous study, pyridinic N, pyrrole N and graphitic N are conducive to improve ORR performance, and the coordination of Fe–N$_x$ may be the active site of the catalyst.[50] Specifically, N-doped changes the electronic structure of graphite carbon, thus promoting the O$_2$ adsorption and destroying O–O bond, which is beneficial to accelerate the ORR process.[51] The results also confirm the formation of Fe and Fe$_3$O$_4$ and the effective introduction of nitrogen into the carbon matrix, which further verifies the results of HRTEM and XRD measurements. Fig. 4e shows that the C 1 s spectrum of Fe/Fe$_3$O$_4$@NC is assigned to four peaks of C–C, C–N, C–O and O–C=O at 284.6, 285.0, 286.4 and 290.2 eV, confirming that the compound structure of biomass derived porous carbon matrix. Furthermore, Fig. 4f shows that the O 1 s XPS spectrum of Fe/Fe$_3$O$_4$@NC is ascribed to Fe–O, C=O, C–OH/C–O–C and C–O at 530.5, 531.7, 532.7 and 533.8 eV, respectively. The high-resolution of C 1s, O 1s and Fe 2p, N 1s XPS spectra in Fe/Fe$_3$O$_4$@C (N-free) and Fe/Fe$_3$O$_4$@NC (Zn-free) catalyst are shown in Fig. S6.† Consequently, not only can iron species be used as active components, but also the combination of nitrogen species in carbon matrix can be improved. It is considered that the synergy between this special N-doped

carbon structure and active components further promotes the electrocatalytic performance of the Fe/Fe$_3$O$_4$@NC catalyst.

3.2. Electrochemical performance for ORR

The ORR performance of the synthesized materials were measured by cyclic voltammetry (CV) and linear sweep voltammetry (LSV) in 0.1 M Ar- and O$_2$-saturated KOH solution. Fig. 5a first indicates the CV curves that Fe/Fe$_3$O$_4$@NC and Pt/C have obvious oxygen reduction peaks in O$_2$-saturated solution, which suggests the existence of ORR electrocatalytic activity for both catalysts. Next, Pt/C, Fe/Fe$_3$O$_4$@NC, Fe/Fe$_3$O$_4$@NC (Zn-free), NC (Fe-free), Fe/Fe$_3$O$_4$@C (N-free) and Fe$_3$O$_4$@NC catalysts are measured with rotating disk electrode (RDE) at 1600 rpm (in Fig. 5b). The ORR polarization curve and the calculated corresponding bar graph are clearly shown in Fig. S8,† we can see that Fe/Fe$_3$O$_4$@NC catalyst displays good ORR activity with positive $E_{1/2}$ = 0.90 V $vs.$ RHE and supreme J_L = 5.87 mA cm^{-2}, even better than Pt/C catalyst ($E_{1/2}$ = 0.887 V $vs.$ RHE, J_L = 5.78 mA cm^{-2}). It is also demonstrated that the $E_{1/2}$ values of Fe/Fe$_3$O$_4$@NC (Zn-free), NC (Fe-free), Fe/Fe$_3$O$_4$@C (N-free) and Fe$_3$O$_4$@NC modified catalysts are 0.858, 0.697, 0.828 V, and 0.874 $vs.$ RHE, respectively, where J_L are 5.38, 4.43, 4.74 and 5.22 mA cm^{-2}, respectively. Apparently, the catalyst without iron species has the lowest ORR catalytic activity, followed by the
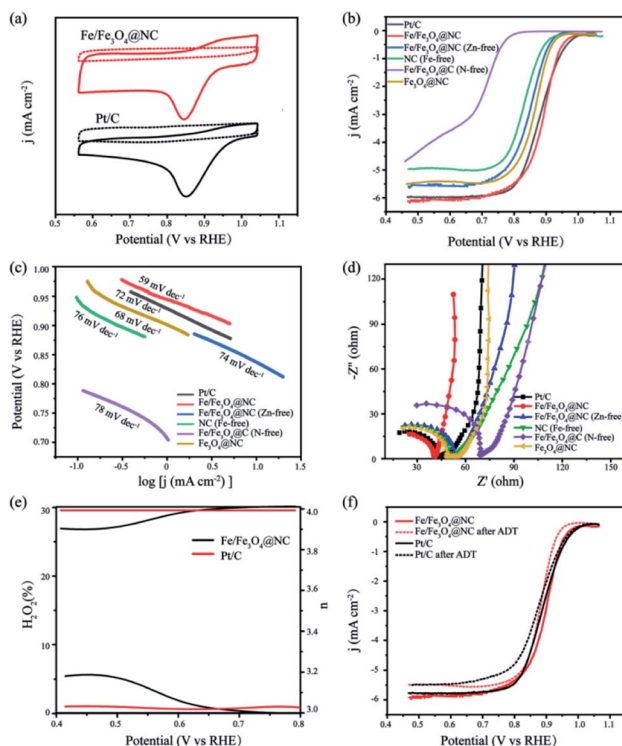

Fig. 5 (a) CV curves of Fe/Fe$_3$O$_4$ @NC and the Pt/C catalysts in Ar- or O$_2$-saturated 0.1 M KOH solution, (b) LSV curves of Pt/C, Fe/Fe$_3$O$_4$@NC, Fe/Fe$_3$O$_4$@NC (Zn-free), Fe/Fe$_3$O$_4$@C (N-free), NC (Fe-free) and Fe$_3$O$_4$@NC catalysts at 1600 rpm, (c) Tafel slopes, (d) EIS plots, (e) the yield of H$_2$O$_2$ and transfer electron numbers, (f) LSV curves before and after ADT test by 5000 CV cycles of Fe/Fe$_3$O$_4$@NC and Pt/C.

catalyst without melamine, and finally the catalyst without zinc nitrate. The results suggest that the Fe/Fe$_3$O$_4$@NC nanoparticles are considered as ORR active component, and the addition of zinc nitrate activator and melamine intercalation agent can significantly improve the electrocatalytic activity of ORR. Compared with previously reported biomass-derived carbon materials, the Fe/Fe$_3$O$_4$@NC catalyst shows outstanding ORR catalytic activity, as summarized in Table S2.† Furthermore, the Tafel slope was employed to assess the ORR kinetic of the samples. Fig. 5c shows the values of Fe/Fe$_3$O$_4$@NC is 59 mV dec^{-1}, less than Pt/C, Fe/Fe$_3$O$_4$@NC (Zn-free), NC (Fe-free), Fe/Fe$_3$O$_4$@C (N-free) and Fe$_3$O$_4$@NC (72, 74, 76, 78 and 68 mV dec^{-1}, respectively), explaining that Fe/Fe$_3$O$_4$@NC catalyst has a favourable kinetics for fast electron transfer behaviour during ORR electrocatalysis. The charge transfer resistance (R_{ct}) ability of the catalysts was examined by the electrochemical impedance spectra (EIS). Compared with other catalysts, Fe/Fe$_3$O$_4$@NC achieves the minimum charge resistance and maximum mass transfer efficiency (Fig. 5d), which is consistent with the ORR performance results. The kinetic mechanism of ORR was studied by the rotating ring-disk electrode (RRDE) measurements. The electron transfer number (n) and the hydrogen peroxide yield (H$_2$O$_2$%) of catalysts during electrocatalytic process are calculated by Koutecky–Levich (K–L) equation.[52] Fig. 5e shows the electron transfer number are approximate to 3.93 and 3.96, confirming that Fe/Fe$_3$O$_4$@NC catalyst shows an efficient 4e$^-$ transfer pathway of ORR. Meanwhile, both catalysts show a low H$_2$O$_2$ yields (less than 5%) in the potential range from 0.20 to 0.80 V vs. RHE. The results show that Fe/Fe$_3$O$_4$@NC has outstanding ORR catalytic activity in alkaline electrolyte.

To deeply investigate the enhanced ORR catalytic activity of the catalysts, the cycling stability was performed by accelerated durability test (ADT) in the O$_2$-saturated alkaline solution. Fig. 5f shows that Fe/Fe$_3$O$_4$@NC has only a slight negative shift by 17 mV after 5000 CV cycles. Besides that, the structural stability after ADT test is further observed in Fig. S9,† the morphology of Fe/Fe$_3$O$_4$@NC catalyst almost maintains the multilayer two-dimensional porous carbon structure. The robust stability of Fe/Fe$_3$O$_4$@NC catalyst derives from the combination of nitrogen doping and carbon matrix, and the graphitized carbon also keeps the active components away from agglomeration during the electrolysis process.

4. Conclusions

In summary, this work put forward a simple and feasible approach to successfully prepare Fe/Fe$_3$O$_4$@NC catalyst with α-cellulose powder, zinc nitrate, iron nitrate and melamine as precursors by impregnation–calcination method combined with freeze-drying technique. As a result, the Fe/Fe$_3$O$_4$@NC catalyst shows a large specific surface area and good electronic conductivity under the synergistic effect of zinc nitrate activator and nitrogen doping, so as to better disperse the active components of Fe$_3$O$_4$ nanoparticles. Electrochemical test results further demonstrate that Fe/Fe$_3$O$_4$@NC catalyst exhibits better electrocatalytic ORR activity with positive half-wave potential and limit current density (0.90 V vs. RHE and 5.87

mA cm^{-2}) than Pt/C (0.887 V vs. RHE and 5.78 mA cm^{-2}). Moreover, Fe/Fe$_3$O$_4$@NC shows a nearly 4e$^-$ pathway for ORR, the yield of H$_2$O$_2$ is less than 5%, and it exhibits a decent stability in alkaline medium only 17 mV loss in the half-wave potential after 5000 CV cycles of ADT test. Therefore, Fe/Fe$_3$O$_4$@NC catalyst possesses a potential application prospects in fuel cells, which provides an innovative and sustainable tactics for rational design of other efficient N-doped transition metal-based biomass materials ORR electrocatalysts.

Conflicts of interest

There are no conflicts to declare.

Acknowledgements

References

1 B. E. Logan, B. Hamelers, R. Rozendal, U. Schroder, J. Keller, S. Freguia, P. Aelterman, W. Verstraete and K. Rabaey, Environ. Sci. Technol., 2006, 40, 5181–5192.
2 Z. P. Cano, D. Banham, S. Ye, A. Hintennach, J. Lu, M. Fowler and Z. Chen, Nat. Energy, 2018, 3, 279–289.
3 B. C. Steele and A. Heinzel, Nature, 2001, 414, 345–352.
4 Y. Wang, S. J. Moura, S. G. Advani and A. K. Prasad, Int. J. Hydrogen Energy, 2019, 44, 8479–8492.
5 L. Xing, Chem. Eng. Sci., 2018, 179, 198–213.
6 M. Liu, A. Hu, Y. Ma, G. Wang, L. Zou, X. Chen and H. Yang, J. Electroanal. Chem., 2020, 871, 114267.
7 S. Bandyopadhyay, G. N. Mukherjee and M. G. B. Drew, Inorg. Chim. Acta, 2006, 359, 3243–3251.
8 L. L. Ma, X. Hu, W. J. Liu, H. C. Li, P. K. S. Lam, R. J. Zeng and H. Q. Yu, Chemosphere, 2021, 278, 130508.
9 G.-L. Chai, K. Qiu, M. Qiao, M.-M. Titirici, C. Shang and Z. Guo, Energy Environ. Sci., 2017, 10, 1186–1195.
10 J. Tong, W. Ma, W. Wang, J. Ma, W. Li, L. Bo and H. Fan, J. Electroanal. Chem., 2018, 809, 163–170.
11 S.-W. Park, H.-J. Shin and D.-W. Kim, Inorg. Chem. Front., 2019, 6, 3501–3509.
12 X. Mao, Z. Cao, S. Chen, J. Jia, X. Li, Y. Yin and S. Yang, Int. J. Hydrogen Energy, 2019, 44, 5890–5898.
13 E. C. Tse, C. J. Barile, N. A. Kirchschlager, Y. Li, J. P. Gewargis, S. C. Zimmerman, A. Zimmerman, A. Hosseini and A. Gewirth, Nat. Mater., 2016, 15, 754–759.
14 G. Zhong, M. Xu, S. Xu, X. Fu, W. Liao and Y. Xu, Int. J. Energy Res., 2021, 45, 10393–10408.
15 Y. Zang, H. Zhang, X. Zhang, R. Liu, S. Liu, G. Wang, Y. Zhang and H. Zhao, J. Nano Res., 2016, 9, 2123–2137.
16 C. Cao, L. Wei, G. Wang, J. Liu, Q. Zhai and J. Shen, Inorg. Chem. Front., 2017, 4, 1930–1938.

17 C. H. Choi, S. H. Park and S. I. Woo, *Int. J. Hydrogen Energy*, 2012, **37**, 4563–4570.

18 J. Liu, C. Fan, G. Liu and L. Jiang, *Appl. Surf. Sci.*, 2021, **538**, 148017.

19 X. Lv, Z. Xiao, H. Wang, X. Wang, L. Shan, F. Wang, C. Wei, X. Tang and Y. Chen, *J. Energy Chem.*, 2021, **54**, 626–638.

20 D. Wu, W. Liu, J. Hu, C. Zhu, H. Jing, J. Zhang, C. Hao and Y. Shi, *Mater. Chem. Front.*, 2021, **5**, 3093–3098.

21 C. Li, S. Zhang, Z. Ding, H. Zhou, G. Wang and H. Zhang, *Inorg. Chem. Front.*, 2020, **7**, 3555–3560.

22 D. Li, Z. Han, K. Leng, S. Ma, Y. Wang and J. Bai, *Asian J. Mater. Sci.*, 2021, **56**, 12764–12774.

23 X. Zhang, R. Liu, Y. Zang, G. Liu, S. Liu, G. Wang, Y. Zhang, H. Zhang and H. Zhao, *Inorg. Chem. Front.*, 2016, **3**, 910–918.

24 Y. Wang, X. Jin, Y. Pan, J. Li, N. Guo and R. Wang, *ChemNanoMat*, 2018, **4**, 954–963.

25 S. Kim, K. Choi, Y. Shim, S. Lee and S. Park, *Chemistry*, 2016, **22**, 11435–11440.

26 L. Yang, X. Liu, J. Ding, S. Li, F. Dong, M. Irfan, Y. Li, G. Wang, X. Du and P. Zhang, *Int. J. Hydrogen Energy*, 2019, **44**, 2823–2831.

27 Q. C. Cao, X. B. Ding, F. Li, Y. H. Qin and C. Wang, *J. Colloid Interface Sci.*, 2020, **576**, 139–146.

28 G. Zhang, H. Luo, H. Li, L. Wang, B. Han, H. Zhang, Y. Li, Z. Chang, Y. Kuang and X. Sun, *Nano Energy*, 2016, **26**, 241–247.

29 Y. Li, H. Hu, J. Song, Y. Wu, X. Lv, Z. Xiao, F. Wang and Y. Chen, *Energy Technol.*, 2020, **8**, 2194–4296.

30 D. Xia, R. Wang, Y. Wei, L. Gan and F. Kang, *Mater. Today Energy*, 2018, **9**, 271–278.

31 Y. Cong, G. Xie, X. Meng, H. Wang, F. Meng, C. Li and Q. Zhao, *Ionics*, 2021, **27**, 5287–5295.

32 A. Mahmood, N. Xie, B. Zhao, L. Zhong, Y. Zhang and L. Niu, *Adv. Mater. Interfaces*, 2021, **8**, 2100197.

33 X. Mi, B. Gao, X. Tan, M. Xie, C. Gao, Y. Liu and J. Gao, *Int. J. Hydrogen Energy*, 2021, **46**, 5332–5344.

34 D. Wang, J. Hu, J. Yang, K. Xiao, S. Liang, J. Xu, J. Liu and H. Hou, *Int. J. Hydrogen Energy*, 2020, **45**, 3163–3175.

35 M. Sun, G. Zhang, H. Liu, Y. Liu and J. Li, *Sci. China Mater.*, 2015, **58**, 683–692.

36 R. Hao, J. Chen, Z. Wang, J. Zhang, Q. Gan, Y. Wang, Y. Li, W. Luo, Z. Wang, H. Yuan, C. Yan, W. Zheng, W. Huang, P. Liu, J. Yan, K. Liu, C. Liu and Z. Lu, *Sci. China Mater.*, 2021, **64**, 2987–2996.

37 Y. Zhang, Y. Zhao, M. Ji, H.-m. Zhang, M. Zhang, H. Zhao, M. Cheng, J. Yu, H. Liu, C. Zhu and J. Xu, *Inorg. Chem. Front.*, 2020, **7**, 889–896.

38 J. A. Varnell, E. C. Tse, C. E. Schulz, T. T. Fister, R. T. Haasch, J. Timoshenko, A. I. Frenkel and A. A. Gewirth, *Nat. Commun.*, 2016, **7**, 12582.

39 T. Huang, J. Wei, X. Zhu and E. Zhang, *Int. J. Hydrogen Energy*, 2021, **46**, 30334–30343.

40 G. Liu, B. Wang, P. Ding, Y. Ye, Y. W. Wei, W. Zhu, L. Xu, J. Xia and H. Li, *J. Alloys Compd.*, 2019, **797**, 849–858.

41 S. Li, W. Xu, P. Cheng, J. Luo, D. Zhou, J. Li, R. Li and D. Yuan, *Synth. Met.*, 2017, **223**, 137–144.

42 Y. Liu, J. Ruan, S. Sang, Z. Zhou and Q. Wu, *Electrochim. Acta*, 2016, **215**, 388–397.

43 F. Liu, H. Peng, C. You, Z. Fu, P. Huang, H. Song and S. Liao, *Electrochim. Acta*, 2014, **138**, 353–359.

44 H. Zhou, S. Hong, H. Zhang, Y. Chen, H. Xu, X. Wang, Z. Jiang, S. Chen and Y. Liu, *Appl. Catal., B*, 2019, **256**, 117767.

45 M. Sevilla and A. B. Fuertes, *Carbon*, 2006, **44**, 468–474.

46 J. Chen, D. Wu, Z. Zhou and Y. Huang, *Int. J. Hydrogen Energy*, 2021, **46**, 27576–27584.

47 G. Daniel, T. Kosmala, F. Brombin, M. Mazzucato, A. Facchin, M. C. Dalconi, D. Badocco, P. Pastore, G. Granozzi and C. Durante, *Catalysts*, 2021, **11**, 2073–4344.

48 Y. T. Chan and M. K. Tsai, *Surf. Sci.*, 2018, **677**, 301–305.

49 B. Yuan, G. Nam, P. Li, S. Wang, X. Liu and J. Cho, *Appl. Surf. Sci.*, 2019, **481**, 498–504.

50 X. Chen, L. Wei, Y. Wang, S. Zhai, Z. Chen, S. Tan, Z. Zhou, A. K. Ng, X. Liao and Y. Chen, *Energy Storage Mater.*, 2018, **11**, 134–143.

51 S. Kattel, P. Atanassov and B. Kiefer, *Phys. Chem. Chem. Phys.*, 2014, **16**, 13800–13806.

52 S. Sadeghhassani, L. Samiee, M. R. Ganjali and A. M. Rashidi, *J. Iran. Chem. Soc.*, 2021, **24**, 1735–2428.